JOURNAL OF MATERIALS SCIENCE **35** (2000) 5597–5603

Study of the paramagnetic-antiferromagnetic transition and the $\gamma \longrightarrow \varepsilon$ martensitic transformation in Fe-Mn alloys

LU XING
Department of Materials Science & Engineering, Dalian Railway Institute, Dalian 116028, People's Republic of China; State Key Laboratory for RSA, Institute of Metal Research, Chinese Academy of Science, Shengyang 110015, People's Republic of China
E-mail: luxing@dlrin.edu.cn

QIN ZUOXIANG, ZHANG YANSHENG, WANG XINGYU, LI FENGXIAN
Department of Materials Science & Engineering, Dalian Railway Institute, Dalian 116028, People's Republic of China

DING BINGZHE, HU ZHUANGQI
State Key Laboratory for RSA, Institute of Metal Research, Chinese Academy of Science, Shengyang 110015, People's Republic of China

The paramagnetic-antiferromagnetic transition and the $\gamma \rightarrow \varepsilon$ martensitic transformation of Fe-Mn (Mn 15–32 wt%) alloys have been investigated by resistivity, dilatometry and X-ray diffraction (XRD). The results show that paramagnetic-antiferromagnetic transition increases the resistivity and the volume of alloys, whereas the $\gamma \rightarrow \varepsilon$ martensitic transformation reduces the resistivity and volume of alloys. The A_f^{ε} that was determined by the dilatometric method is not the temperature that ε martensites in the Fe-Mn alloys have reverse transformed to austenites completely. Mn additions reduce M_s, increase T_N and the lattice parameter of austenite in the Fe-Mn alloys. Both the antiferromagnetic transition and the $\gamma \rightarrow \varepsilon$ martensitic transformation lead to an increase in the lattice parameter of austenite. The lattice parameters both above T_N and below T_N decrease linearly with temperature. The lattice parameter below M_s increases first and then decreases. Moreover, the α (110) and ε (002) atomic planes in the Fe-15Mn-0.15C alloy are separated into two peaks: 2θ for $\varepsilon(002)$ is 44.16°, 2θ for $\alpha(110)$ is 44.47°. *© 2000 Kluwer Academic Publishers*

1. Introduction

In addition to Ni, Mn is another fcc(γ) stabilizing element. Consequently, material scientists have long considered Fe-Mn based austenitic steel as a possible alternative to Fe-Ni based austenitic-steel. Among the high manganese austenitic-steels, these groups may be distinguished: Fe-Mn-Cr, Fe-Mn-Al and Fe-Mn-C. The Fe-Mn-Cr has been used as heat-resistance steel, stainless steel, nonmagnetic retaining ring steel and so on. It is also suitable for fusion reactor structural applications as regards a reduced activation property [1, 2]. The high nitrogen alloying is essential to Fe-Mn-Cr alloy due to the relatively low strength of the Fe-Mn-Cr alloys [3, 4]. In the Fe-Mn-Al alloys, Al strongly depresses the $\gamma \rightarrow \varepsilon$ martensitic transformation, improves the corrosion-resistance and oxidation-resisting properties. Some researchers expected to develop a Fe-Mn-Al stainless steel [5]. However, the more recent experiments have proven it unfavorable [6, 7]. Nevertheless, Fe-Mn-Al alloy is suitable for cryogenic and nonmagnetic applications [8, 9]. A heat-resistance and high-strength steel based on Fe-Mn-Al alloy was also successfully developed [10]. Hadfield steel (Fe-Mn-C) is the most important alloy based on Fe-Mn system, which is characterized by the hardening of surface due to the induced $\gamma \rightarrow \varepsilon$ martensitic transformation and deformed twins upon impacting [11, 12].

The paramagnetic-antiferromagnetic transition in the Fe-Mn alloy is an interesting phenomenon to attract both material scientists and physicists. For physicists, Fe-Mn alloy is another typical gap-type itinerant antiferromagnet besides Cr [13, 14]. In the past two decades, Zhang [15–17] has investigated the effects of Al, Si and Ge on the paramagnetic-antiferromagnetic transition of the Fe-Mn system, and a weakening of the itinerant electron characteristics of anti-ferromagnetism by doping with these elements was found. Recently, Fe-Mn alloy has been used as biased layer in spin-valve multi-layer structure [18, 19]. Material scientists take advantage of the paramagnetic-antiferromagnetic transition to develop Fe-Mn based functional alloys, such as precision resistance alloy, Covar alloy and so on [20, 21].

As far as the Fe-Mn binary alloys are concerned, there mainly exists ε and α phases between 10–15wt%Mn; γ and ε phase between 15–28wt%Mn; γ phase above 28wt%Mn. Mn depresses both the $\gamma \rightarrow \varepsilon$ martensitic transformation and $\gamma \rightarrow \alpha$ martensitic transformation [22]. The strain induced $\gamma \rightarrow \varepsilon$ martensitic transformation and its reverse transformation in Fe-Mn binary alloys can only give rise to a weak shape memory effect (SME) [23]. In 1982, Sato *et al*. [24] obtained complete SME by adding 1%Si to Fe-30Mn alloy. This important discovery stimulated the investigation on $\gamma \rightarrow \varepsilon$ martensitic transformation in Fe-Mn alloys. Since then, Fe-Mn-Si shape memory alloys have been the most active subject in the study of Fe-Mn based alloys [25–30].

The low stacking fault energy in Fe-Mn alloy makes it easy to decompose a perfect dislocation into partial dislocations. The $\gamma \rightarrow \varepsilon$ martensitic transformation occurs as a Shockley partial dislocation gets across every second (111) layer. Therefore, transmission electron microscopy (TEM) is the most useful tool to observe the stacking faults, ε martensite and twins in Fe-Mn alloys. High-resolution electron microscopy (HREM) has also been successfully used in the study of Fe-Mn based alloys [29, 30]. These observations are essential to the understanding of the mechanism of the $\gamma \rightarrow \varepsilon$ martensitic transformation and its reversion transformation. Relatively, there are only a few reports on the X-ray diffraction (XRD) study in the Fe-Mn system [31, 32]. The main reason is that XRD can only present the bulk information of structure. Nevertheless, XRD is superior to TEM in determining the crystal structure and lattice parameter precisely. In the present article, we will first discuss the $\gamma \rightarrow \varepsilon$ martensitic transformation and paramagnetic-antiferromagnetic transition behavior of Fe-Mn alloys (Mn 15–32%) by resistivity measurement and dilatometry. Then we study the variation of the lattice parameter of austenite with temperature in Fe-Mn alloys by high temperature XRD, to understand the fine change of crystal size during $\gamma \rightarrow \varepsilon$ martensitic transformation and paramagnetic-antiferromagnetic transition in Fe-Mn alloys.

2. Experiment methods

The alloys were made by induction melting in an argon gas atmosphere. The ingots were forged into 20×20 mm^2 rods. Table I listed the chemical compositions together with the Néel temperatures (T_N) measured by MB-2 magnetic balance. The rods were solid solution treated at 1273 K for 1 h, followed by water quenching to obtain homogeneous structure. The sample for dilatometry ($\phi 3.5 \times 50$ mm^2) and the sample for XRD experiments ($1.5 \times 15 \times 23$ mm^3) were obtained by electric spark cutting. The XRD samples were grinded and polished mechanically first, and then electropolished in a solution of 10 pct $HClO_4$ and 90pct CH_3COOH. The thermal expansion curve was measured in a sequence of 500 K → 100 K → 500 K by a DP-49 dilatometer equipped with a cryostat, and an electrolyzed copper rod was used as a temperature calibrator. The X-ray diffraction measurements were performed using a Rigaku D/Max-rA diffractometer with copper radiation using 50 kV voltage and 140 mA current. In order to reduce the oxidation of sample, the high temperature attachment of diffractometer was evacuated by a rotation pump. After being heated to 573 K (523 K for Fe-24Mn and Fe-32Mn alloys) at a heating rate of 20 K/minute, the XRD sample was cooled at a rate of 5 K/minute. The XRD spectrum was measured at each selected temperature with a fluctuation of about ±1 K. The scanning rate of the diffractometer was 0.02°/step, 10 second/step when a lattice parameter was measured. The lattice parameter of austenite was calculated by the averaging that of $\gamma(111)$, $\gamma(200)$, $\gamma(220)$ and $\gamma(311)$, due to the weakness of reflection at higher angles in the high temperature measurements. The lattice parameter of α martensite was calculated by averaging that of $\alpha(110)$ and $\alpha(211)$. The lattice parameters of ε martensite were calculated by averaging that of $\varepsilon(002)$, $\varepsilon(101)$, $\varepsilon(102)$, $\varepsilon(110)$ and $\varepsilon(112)$. The scanning rate was 0.05°/step, 0.2 second/step, when a full XRD spectrum between 40° and 100° was determined. The lattice parameters measured at high temperature attachment were corrected by comparing both results measured at high temperature attachment and standard sample attachment with a graphite monochromator at room temperature. The standard sample attachment had been calibrated using standard Si sample.

TABLE I Chemical compositions (wt%) of alloys tested

Alloy	Mn	C	Si	P	S	T_N(K)
1	15.29	0.15		<0.005	<0.003	
2	19.56	0.16	<0.005	<0.005	0.009	375
3	24.09	0.19				400
4	32.65	0.076				

3. Experimental results and discussion

3.1. Resistivity

Fig. 1 shows the resistivity versus temperature relation of alloys during 500 K → 100 K → 500 K thermal cycle. The resistivity of the Fe-Mn alloys increases with increasing in Mn content. There is an obvious break on the cooling curve of Fe-15Mn alloy, which is the start temperature of $\gamma \rightarrow \varepsilon$ martensitic transformation (M_S^{ε}). A resistivity loop is formed in the thermal cycle because of the lagging of $\varepsilon \rightarrow \gamma$ reverse transformation. A larger loop area represents a larger amount of martensite formed upon cooling in the alloy. It should be mentioned that the resistivity of ε martensite in the Fe-Mn alloys is smaller than that of austenite [33], while the resistivity of ε martensite is larger than that of austenite in Fe-Mn-Si alloy [34]. Moreover, the paramagnetic-antiferromagnetic transition temperature could not be determined by means of the resistive measurement, which implies that the Néel temperature (T_N) of Fe-15Mn alloy is close to the M_s of the alloy. The resistivity of the Fe-20Mn alloy is similar to that of Fe-15Mn alloy. The break on cooling line is not as evident as that of Fe-15Mn alloy, which also means that the amount of martensite formed upon cooling is smaller than that in the later alloy. The M_s of Fe-20Mn alloy determined from the cooling curve is also lower than that of Fe-15Mn

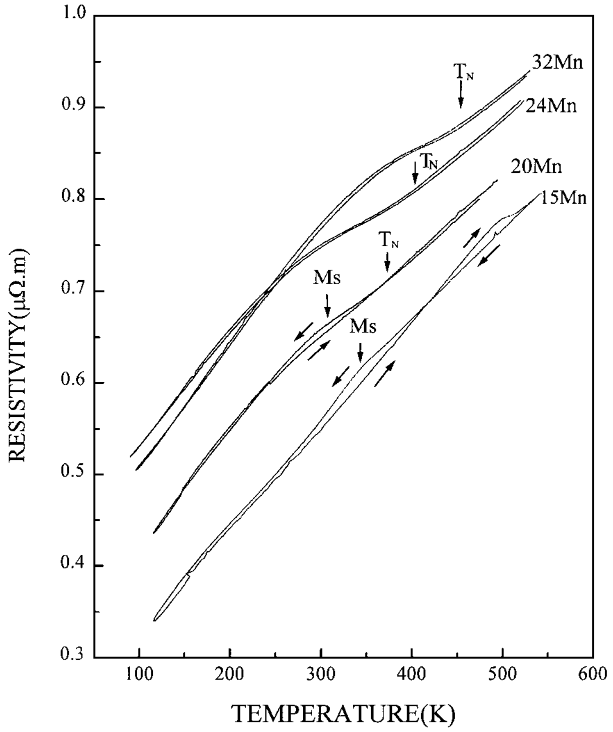

Figure 1 Resistivity vs. temperature of Fe-Mn alloys upon 500 K → 100 K → 500 K thermal cycle.

alloy. In addition to the $\gamma \rightarrow \varepsilon$ martensitic transformation, the paramagnetic-antiferromagnetic transition can also been observed in the Fe-20Mn alloy. The increase in resistivity below T_N compared with the normal decrease of resistivity upon cooling is originated by the paramagnetic → antiferromagnetic transition, which should be attributed to scattering of antiferromagnetic spin ordering on the conducting electrons [35]. The temperature dependence of resistivity for Fe-24Mn and Fe-32Mn alloys are different from that of the former two alloys: their resistivity curves both upon cooling and heating superimposes almost completely. The $\gamma \rightarrow \varepsilon$ martensitic transformation could not been distinguished in the measurement of resistivity for the alloys. The result verifies that Mn additions decrease the M_s and thus depresses the $\gamma \rightarrow \varepsilon$ martensitic transformation in Fe-Mn alloys [22]. The paramagnetic-antiferromagnetic transition of the two alloys has been clearly detected in the resistivity versus temperature measurement. The reason that the resistivity of Fe-32Mn alloy decreases more rapidly at lower temperature is its lower C content (0.076%) compared with the other alloys (≈0.16%) [36]. The temperature at which the resistivity starts to deviate from the linear relation upon cooling is generally considered as T_N [35], as shown in Fig. 1, where it can be found that Mn increases the T_N in Fe-Mn alloy [13].

3.2. Dilatometry

Fig. 2a presents the dilatometric measurement in the Fe-15Mn alloy during 500 K → 100 K → 500 K thermal cycle. The process of $\gamma \rightarrow \varepsilon$ martensitic transformation upon cooling and $\varepsilon \rightarrow \gamma$ reverse transformation upon heating can be observed clearly. The contraction of Fe-15Mn alloy during $\gamma \rightarrow \varepsilon$ martensitic transformation indicate that the volume of ε martensite is smaller than that of γ phase. The dilatometrical result for the Fe-20Mn alloy is similar to that of Fe-15Mn alloy, besides that its loop area is smaller than that of the later, as shown in Fig. 2b. It means the less amount of martensite formed in Fe-20Mn alloy. In addition, the M_S of Fe-20Mn alloy is also lower than that of Fe-15Mn alloy, which agrees with the result of resistivity. Moreover, there is a small upside inflexion on the cooling curve just above M_S of Fe-20Mn alloy, which is caused by paramagnetic → antiferromagnetic transition. Fig. 2c shows that there exists $\gamma \rightarrow \varepsilon$ martensitic transformation in Fe-24Mn alloy above 100 K, although the amount of martensite formed is much less than that of the alloys just described. It indicates that the dilatometry is a more sensitive method to detect the $\gamma \rightarrow \varepsilon$ martensitic transformation in Fe-Mn alloys than resistivity measurement. In Fig. 2c, the decrease of thermal expansion coefficient caused by paramagnetic → antiferromagnetic transition can also be found. As far as the Fe-32Mn alloy is concerned, the dilatometric curves upon both cooling and heating superimpose completely, as shown in Fig. 2d. It suggests that the paramagnetic-antiferromagnetic transition is the only transition occurring between 500 K and 100 K for the alloy. A positive antiferromagnetic magnetostriction leads a clear inflexion on the dilatometrical curve [20], and T_N is determined as the temperature which dilatometric curve begins to deviate from the linear variation upon cooling, as shown in Fig. 2. From the present dilatometric measurements, we can conclude that the $\gamma \rightarrow \varepsilon$ martensitic transformation reduces the volume of Fe-Mn alloy, whereas the paramagnetic → antiferromagnetic transition increases it.

3.3. Room temperature X-ray diffraction

Fig. 3 shows the full XRD spectrum between 40–100° for the alloys. As shown in the Fig. 3, besides γ and ε, there also occurs the α phase in the Fe-15Mn alloy. However, only the γ and ε phases exist in Fe-20Mn alloy. The peak of ε (101) is clearly visible for Fe-24Mn alloy, but its area is very small compared with that in the Fe-15Mn and Fe-20Mn alloys. It means that there is only a small amount of ε martensite in the alloy. In the case of Fe-32Mn alloy, the peak of ε (101) disappears completely, which implies that there only exists single γ phase. The results of XRD experiments agree that of the resistivity measurement and dilatometry well. The lattice parameters of γ, ε and α phase have been measured precisely at a slow scanning rate, as shown in Table II. It is found that the lattice parameter of γ phase increases with the Mn content. The values in Table II are a little higher than in the classic result of Schmidt [37], which might be ascribed to the influence of the C content in the present alloys. In his work, the peak of ε(002) superposes that of α(110) for the Fe-Mn alloy. However, in present investigation, these two peaks have been separated, as shown in Fig. 4. According to the root-mean-square results in calculating the lattice parameter of ε and α phases, as shown in Table III, it is suggested that the low angle peak should be ε(002),

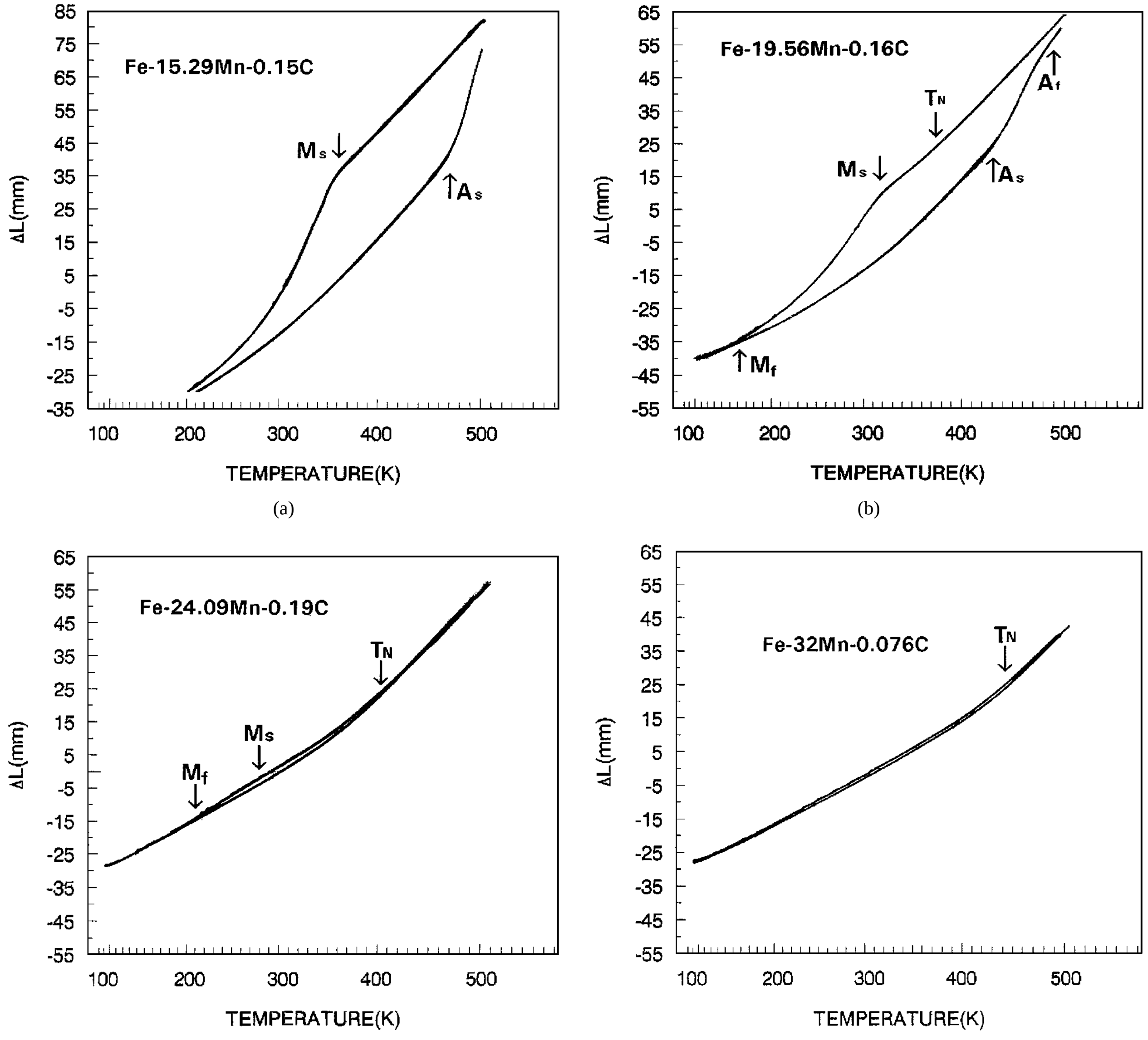

(a) (b) (c) (d)

Figure 2 Thermal expansion of Fe-Mn alloys upon 500 K → 100 K → 500 K thermal cycle, (a) Fe-15Mn (b) Fe-20Mn (c) Fe-24Mn (d) Fe-32Mn. The high temperature XRD will show that there still exist ε martensites above A_f for Fe-15Mn and Fe-20Mn alloys.

$2\theta = 44.16^\circ$, and the high angle peak should be $\alpha(110)$, $2\theta = 44.47^\circ$. The separation of the peaks is probably due to the influence of C atoms in the present investigation, or the lower resolution of the Debye diffractometer used by Schmidt [37] compared with the present Rigaku D/Max-rA diffractometer used by us.

3.4. High temperature XRD

On the base of the resistivity and dilatometric measurements, it is estimated that the $\varepsilon \rightarrow \gamma$ reverse transformation of the alloys should have completed as the alloys are heated above 523 K. However, high temperature XRD shows that ε martensites still exist in the Fe-15Mn and Fe-20Mn alloys although the temperature is as high as 573 K, as presented in Figs 5 and 6. A. Sato [26, 38] and other authors [23] have already proposed that the α martensite introduced and ε martensite trapped by the other ε martensite plates prevent the $\varepsilon \rightarrow \gamma$ reverse transformation and increase the temperature of reversible motion of partial dislocations. The present high XRD measurements confirm their results on the thermal induced $\gamma \rightarrow \varepsilon$ martensitic transformation, and also show the insufficiency of dilatometrical methods in determining the A_f^ε. In another words, the A_f^ε temperature determined from the dilatometric curve only represents the finishing of reverse transformation for those ε martensites that transform to austenite easily. Those ε martensites, which are related to α martensite or trapped by other ε martensite plates, will transform slowly at higher temperature. In order to prevent excess oxidation and demanganization of sample surface, the highest measuring temperatures for the Fe-15Mn and Fe-20Mn alloys are chosen to be 573 K. Fig. 7 shows the $\gamma \rightarrow \varepsilon$ martensitic transformation for the Fe-15Mn alloy. Between 573 K and M_s of the Fe-15Mn alloy, there is only a little change in the peak area of ε phase. However, as the alloy is cooled below M_s, the peak area of γ (111) decreases, and the overlapped peak of $\varepsilon(002)$ and $\alpha(110)$ increases, as shown in Fig. 7. It should be noted that the $\varepsilon(002)$ and $\alpha(110)$ overlapped peaks cannot be distinguished in Fig. 7, since the resolution of the high temperature XRD measurements is much inferior

TABLE II Lattice parameter of γ, ε and α phases in Fe-Mn alloys at room temperature

	γ	ε		α
Alloy	*a*	*a*	*c*	*a*
1	0.3595	0.2539	0.4093	0.288
2	0.3604	0.2535	0.4102	
3	0.3606	0.2548	0.4085	
4	0.3614			

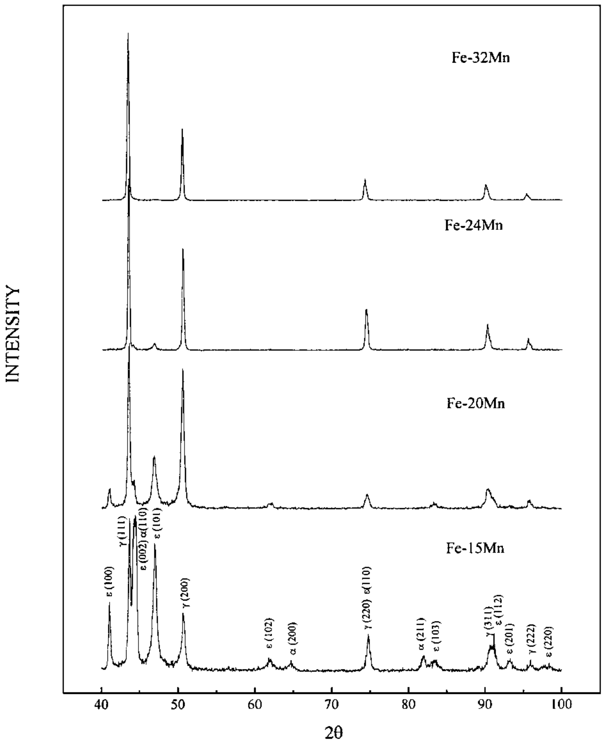

Figure 3 XRD spectrum of Fe-Mn alloys showing the structure change of Fe-Mn alloys with Mn-content at room temperature.

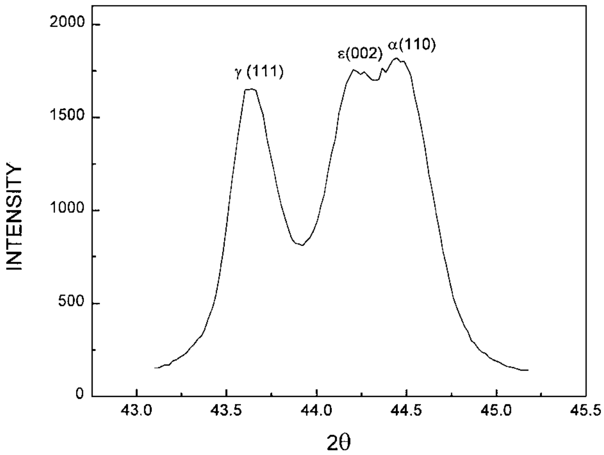

Figure 4 XRD spectrum of Fe-15Mn-0.15C alloy at room temperature, showing peak separation of $\varepsilon(002)$ and $\alpha(110)$.

to that of standard ambient XRD. Several researchers [33, 38, 39] have reported that the start temperature of $\alpha \rightarrow \gamma$ reverse transformation in Fe-Mn alloys is higher than 700 K, which means that the α martensite is stable during the present thermal cycle. Therefore, the change of the peaks in Fig. 7 is exclusively originated from the $\gamma \rightarrow \varepsilon$ martensitic transformation.

TABLE III Root-mean-square results by different fitting procedure for $\alpha(110)$ and $\varepsilon(002)$ of Fe-15Mn-0.15C alloy

Fitting procedure	Single peak fitting	Double peak fitting (low angle be α)	Double peak fitting (low angle be ε
oot-mean-square of ε	913×10^{-3}	411×10^{-3}	761×10^{-3}
oot-mean-square of α	62×10^{-3}	099×10^{-3}	759×10^{-3}

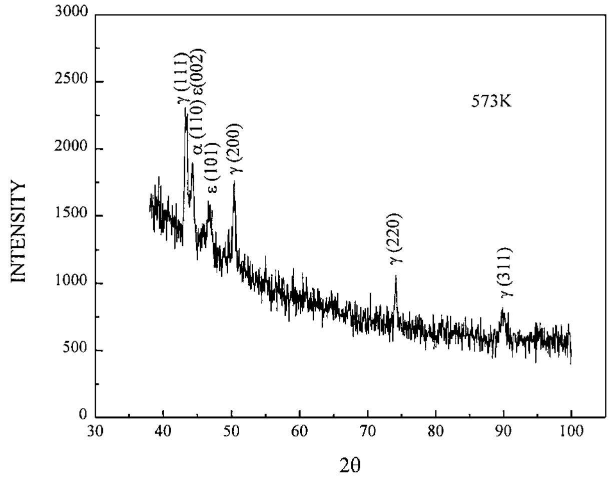

Figure 5 XRD spectrum of Fe-15Mn-0.15C alloy showing the existence of ε martensite at 573 K.

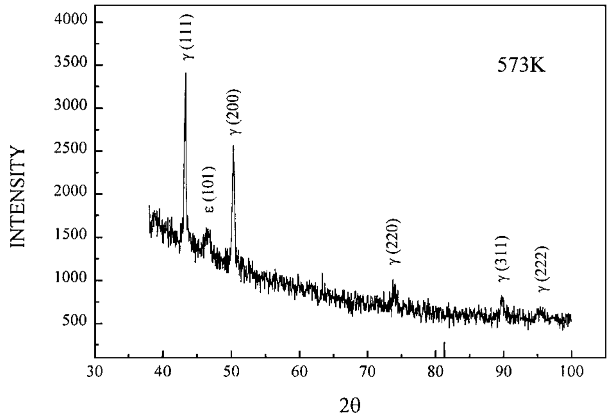

Figure 6 XRD spectrum of Fe-20Mn-0.16C alloy showing the existence of ε martensite at 573 K.

Fig. 8 shows the relation between the lattice parameter of austenite and temperature upon cooling. In the cases of the Fe-32Mn and Fe-24Mn alloys, two linear relations have been divided by T_N; the slope of the linear relation below T_N is smaller than that above T_N. This is consistent with the dilatometric results just described and previously reported [40] result by XRD. The thermal expansion coefficients both above T_N and below T_N have been calculated according to the slopes, as shown in Table IV. The results determined by lattice parameter are very close to those determined by dilatometric measurements. The T_N of Fe-32Mn alloy is the highest among the four alloys, so the temperature range measured above T_N is relative narrow; the error in the thermal expansion coefficient is consequently larger. The phase transformation temperatures measured by resistivity, dilatometry and XRD are also

TABLE IV Phase transformation temperature (K) and thermal expansion coefficient (α) of Fe-Mn alloys (10^{-6}/K)

	T_N		M_s			A_s	$\alpha(>T_N)$		$\alpha(<T_N)$	
Alloy	R	D	XRD	R	D	D	D	XRD	D	XRD
1				340	361	470	20.5	19.8		
2	372			306	319	427	20.5	18.2		
3	401	403	395		280		20.3	18.7	11.2	9.1
4	453	446	448				18.3	22.8	8.8	8.8

*R is resistive measurement, D dilatometry, and XRD X-ray diffraction.

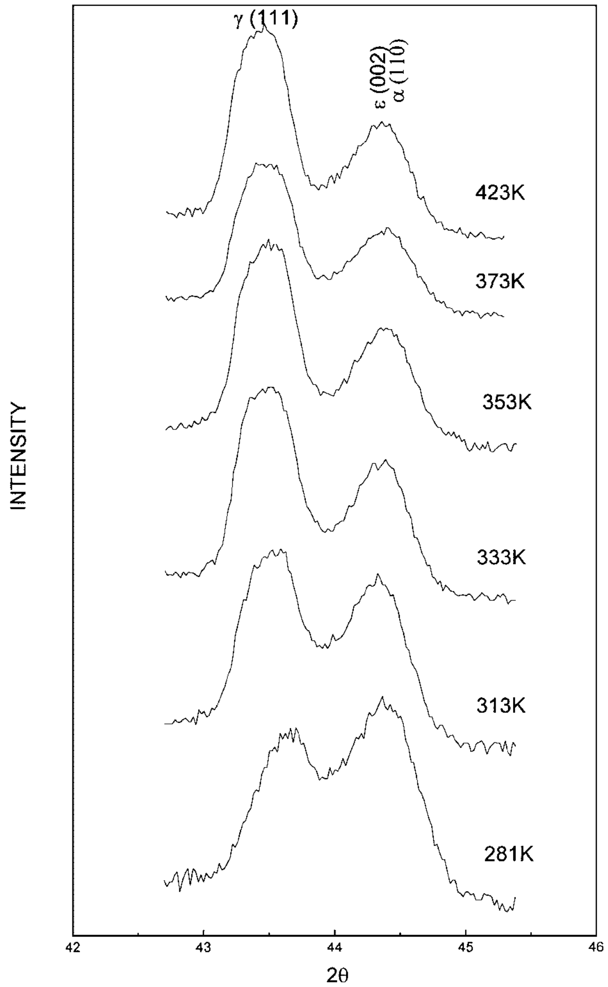

Figure 7 XRD spectrum of Fe-15Mn-0.15C alloy showing the formation process of ε martensite.

listed in Table IV. For the Fe-15Mn and Fe-20Mn alloys in which $\gamma \rightarrow \varepsilon$ martensitic transformation occurs considerably, the change of the lattice parameter of austenite with temperature is quite different from that of the Fe-24Mn and Fe-32Mn alloys. An approximate linear relation above M_S remains for two alloys. However, as the temperature decreases below M_S, the lattice parameter of austenite seems to be constant, even increases a little. Then it decreases again as the alloy is cooled to lower temperature. In other words, the $\gamma \rightarrow \varepsilon$ martensitic transformation has resulted in a nonlinear variation of the austenitic lattice parameter with temperature. The reason may be the decreasing of the volume of ε martensite compared with that of austenite. For example, on the average, twice the spacing of the $(111)_\gamma$ of Fe-20Mn alloy in the present investigation is 0.4162 nm, while the length of the C axis for the ε martensite is only 0.4102 nm. Moreover, the length of the $\langle 110\rangle_\gamma$ axis is 0.2548 nm, while the length of $\langle 100\rangle_\varepsilon$ axis is 0.2535 nm. Therefore, as the $\gamma \rightarrow \varepsilon$ martensitic transformation occurs, not only the two sides but also the longitudinal direction of the ε martensite will subject to tension stress, as shown in Fig. 9. The tension stress leads to the contraction of the alloy, and at same time, the increasing of lattice parameter of austenite to self-accommodate the local environment of different grain. Besides, the T_N and M_S of these two alloys are too close each other; the positive antiferromagnetic magnetostriction can not be distinguished clearly. Nevertheless, the nonlinear behavior of the lattice parameter of austenite below M_S should include its contribution, although a positive antiferromagnetic magnetostriction can not make a nonlinear change of lattice parameter [41].

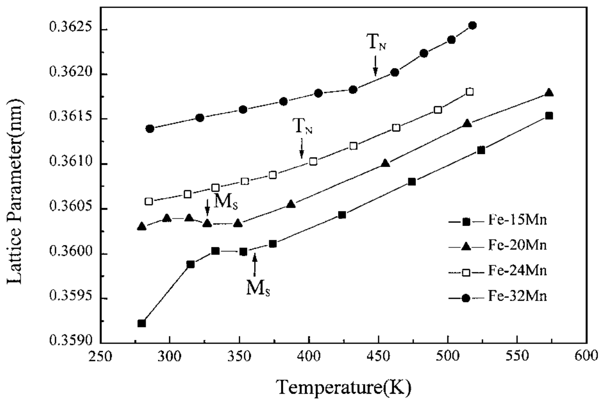

Figure 8 Lattice parameter of austenite vs. temperature for Fe-Mn alloys. M_s is the data determined by dilatometrical measurement. T_N is determined by the intersection of linear relations above and below T_N in the figure.

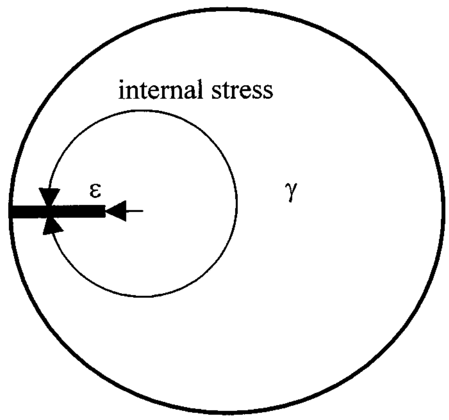

Figure 9 Schematic drawing to explain the increase of the lattice parameter in austenite upon $\gamma \rightarrow \varepsilon$ martensitic transformation. The internal tensive stress due to smaller volume of ε martensite compared with that of γ results in the increase of lattice parameter of austenite.

4. Conclusion

The paramagnetic-antiferromagnetic transition and the $\gamma \rightarrow \varepsilon$ martensitic transformation in Fe-Mn alloys have been investigated by means of resistivity, dilatometry and XRD. The experimental results can be summarized as follows:

(1) Both resistive and dilatometric methods can be employed in the study of the paramagnetic-antiferromagnetic transition and the $\gamma \rightarrow \varepsilon$ martensitic transformation in Fe-Mn alloys. The paramagnetic-antiferromagnetic transition leads to an increase in the resistivity and the volume of the alloy, whereas the $\gamma \rightarrow \varepsilon$ martensitic transformation leads to a decrease in resistivity and volume of alloys in the Fe-Mn system. Dilatometry is a more sensitive method to detect the $\gamma \rightarrow \varepsilon$ martensitic transformation than resistivity. However, high temperature XRD shows that the A_f determined by the dilatometric method does not represent the temperature at which all the ε martensites have transformed to austenite.

(2) Mn additions decrease the $\gamma \rightarrow \varepsilon$ martensitic transformation and the $\gamma \rightarrow \alpha$ martensitic transformation, increases the resistivity, T_N and the lattice parameter of austenite in the Fe-Mn alloys. There are α, ε and γ phases in the Fe-15Mn-0.15C alloy; γ and ε phases in the Fe-20Mn-0.16C alloy; a small amount of the ε phase in Fe-24Mn-0.19C alloy; single γ phase in Fe-32Mn-0.076C alloy. For the Fe-15Mn-0.15C alloy, the peak of $\alpha(110)$ is separated from peak of $\varepsilon(002)$: $2\theta = 44.16^\circ$ for $\alpha(110)$, $2\theta = 44.47^\circ$ for $\varepsilon(002)$.

(3) Both the paramagnetic-antiferromagnetic transition and the $\gamma \rightarrow \varepsilon$ martensitic transformation increase the lattice parameter of austenite in the Fe-Mn alloys. The lattice parameter of austenite above T_N and below T_N changes linearly with temperature. However, the anomalous expansion originated from the $\gamma \rightarrow \varepsilon$ martensitic transformation makes the lattice parameter of austenite increase first, then decrease again. The smaller volume of the ε martensite compared with austenite may be responsible for the anomalous expansion of austenite during $\gamma \rightarrow \varepsilon$ martensitic transformation.

Acknowledgments

The project has been supported by the National Natural Science Foundation of China under grant 59601007. The authors would express thanks to Mr. Gao Zhongming and Mr. Xu Yue of Ji Lin University in X-ray diffraction experiment.

References

1. D. G. RICKERBY and G. PIATTI, *Mater. Sci. Techno.* **7** (1991) 71.
2. F. ABE, H. ARAKI and T. NODA, *ibid.* **4** (1988) 885.
3. S. C. LIU, T. HASHIDA, H. TAKAHASHI, H. KUWANO and Y. HAMAGUCHI, *Metall. Mater. Trans.* **29** (1998) 791.
4. Y. TOMOTA, Y. XIA and K. INOUE, *Acta Mater.* **46** (1998) 1577.
5. S. K. BANERJI, *Met. Prog.* **118**(4) (1978) 59.
6. X. M. ZHU and Y. S. ZHANG, *Corrosion* **54** (1998) 3.
7. W. T. CHAI, J. B. DUH and J. T. LEE, *J. Mater. Sci.* **22** (1987) 3517.
8. J. S. YE, *Acta Metall. Sinica* **13** (1977) 149 (in Chinese).
9. Y. S. ZHANG, *ibid.* **19** (1983) A262 (in Chinese).
10. Y. S. ZHANG, F. T. ZHANG, Y. H. GAO and G. Y. WANG, *ibid.* **20** (1984) A1 (in Chinese).
11. T. N. YAO, *Steel and Iron* **27**(12) (1992) 68 (in Chinese).
12. B. K. ZUIDEMA, D. K. SUBRAMANYAM and W. C. LESTIE, *Metall. Trans.* **18A** (1987) 1629.
13. Y. ENDOH and Y. ISHIKAWA, *J. Phys. Soc. Japan* **30** (1971) 1614.
14. S. ASANO and J. YAMASHITA, *ibid.* **31** (1971) 1000.
15. Y. S. ZHANG, *Acta Metall. Sinica* **22** (1986) A470.
16. *Idem.*, *J. Phys. F: Met. Phys.* **18** (1988) L229.
17. *Idem.*, *J. Phys.: Condens. Matter* **2** (1990) 10033.
18. M. F. GILLIES, J. N. CHAPMAN and J. C. S. KOOLS, *J. Appl. Phys.* **78** (1995) 5554.
19. C. JIN, Y. Z. WU, G. S. DONG and X. F. JIN, *Acta Phys. Sinica* **48** (1999) 289 (in Chinese).
20. Y. S. ZHANG, *Bulletin of Sci. and Tech.* **9**(1) (1993) 6 (in Chinese).
21. *Idem.*, China Patent 1990 No 19905362.
22. A. HOLDEN, J. D. BOLTON and E. R. PETTY, *J. Iron Steel Inst.* (1971) 721.
23. K. ENAMI, A. NAGASAWA and S. NENNO, *Scripta Metall.* **9** (1975) 941.
24. A. SATO, E. CHISHIMA, K. SOMA and T. MORI, *Acta Metall.* **30** (1982) 1177.
25. A. SATO, E, CHISHIMA, Y. YAMAJI and T. MORI, *ibid.* **32** (1984) 539.
26. A. SATO, Y. YAMAJI and T. MORI, *ibid.* **34** (1986) 287.
27. M. MURAKAMI, H. OTSUKA, H. G. SUZUKI and S. MATSUDA, in Proc. Int. Conf. Martensitic Transformation, Nara, Japan, 1986 (Japan Inst. Metals, 1987) p. 985
28. J. H. YANG and C. M. WAYMAN, *Metall. Trans.* **23A** (1992) 1431.
29. K. OGAWA and S. KAJIWARA, *Mater. Trans. JIM* **34** (1993) 1169.
30. J. P. PUTAUX and J. P. CHEVALIER, *Acta Mater.* **44** (1996) 1701.
31. B. H. JIANG, X. QI, S. X. YANG, W. M. ZHOU and T. Y. HSU, *ibid.* **46** (1998) 501.
32. O. MATSUMURA, S. FURUSAKO, T. FUKAWA and H. OTSUKA, *ISIJ Intel.* **36** (1996) 1103.
33. S. COTES, M. SADE and A. FERNANDEZ GUILLERMET, *Metall. Mater. Trans.* **26A** (1995) 1957.
34. Z. X. QIN, M. P. YU and Y. S. ZHANG, *J. Mater. Sci.* **31** (1996) 2311.
35. X. LU and Y. S. ZHANG, *J. Phys. D: Appl. Phys.* **29** (1996) 1428.
36. X. LU, Z. X. QIN, Y. S. ZHANG, X. Y. WANG, F. X. LI, B. Z. PING and Z. Q. HU, *J. Mater. Sci. Tech.* **16** (3) (2000) 297.
37. V. W. SCHMIDT, *Arch. Eisenh.* **3** (1929) 293.
38. Y. HOSHINO, S. NAKAMURA, N. ISHIKAWA, Y. YAMAJI, S. MATSUMOTO, Y. TANAKA and A. SATO, *Mater. Trans. JIM* **33** (1992) 253.
39. M. TOLBA-SALLAM, D. GEORGEAULT and G. CIZERON, *Script. Metall.* **15** (1981) 849.
40. H. UMEBAYASHI and Y. ISHIKAWA, *J. Phys. Soc. Japan* **21** (1966) 1281.
41. X. LU, Z. X. QIN, Y. S. ZHANG, B. Z. DING and Z. Q. HU, *Script. Mater.* **42** (2000) 433.

Received 29 September 1999
and accepted 2 May 2000